Vol. 34 (2003) *ACTA PHYSICA POLONICA B* No 2

CONTROL OF MOTT TRANSITION IN TRANSITION-METAL OXIDES*

S. Miyasaka

Department of Applied Physics, University of Tokyo, Tokyo 113-8656, Japan

Y. Taguchi

Institute for Material Research, Tohoku University, Sendai 980-8575, Japan

and Y. Tokura

Department of Applied Physics, University of Tokyo, Tokyo 113-8656, Japan
Correlated Electron Research Center (CERC) National Institute of Advanced
Industrial Science and Technology (AIST), Tsukuba 305-8562, Japan
Spin Superstructure Project, ERATO, Japan Science and Technology
Corporation (JST), Tsukuba 305-8562, Japan

(Received July 10, 2002)

Late experimental investigations on the filling-control Mott transition are reviewed by taking examples of the perovskite Ti, V, and Mn oxides with controlled one-electron bandwidth. The complex interplay among the spin, charge, and orbital degrees of freedom is laid emphasis to elucidate anomalous features of the barely metallic phase close to the Mott transition point.

PACS numbers: 71.30.+h, 72.15.–v, 75.30.Kz

1. Introduction

Since the discovery of high-temperature superconductivity in cuprates with perovskite-related structures, the research on the Mott transition in transition-metal oxides (TMOs) has been accelerated [1]. Some classic TMOs have also been revisited and new aspects, *e.g.* a mutual interplay among the charge, spin, and orbital degrees of freedom, have been revealed. For the

---

[*] Presented at the International Conference on Strongly Correlated Electron Systems, (SCES 02), Cracow, Poland, July 10–13, 2002.

purpose, the perovskite structure (AMO_3) has been particularly useful because the control of the two important parameters in the correlated electron system, band-filling and bandwidth (see Fig. 1), is capable with use of the compositional change of the perovskite *A*-site (non-TMO site).

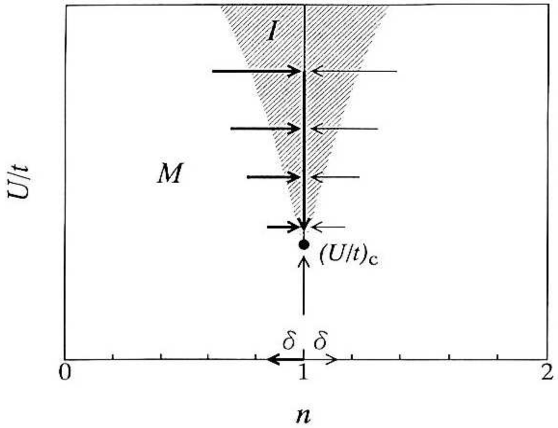

Fig. 1. Metal–insulator phase diagram based on the Hubbard model in the plane of U/t and filling n. I and M denote correlated insulator and metal. Arrows indicate the routes of filling-control and bandwidth-control metal–insulator transitions.

The distortion of the bond angle M-O-M depends on the ionic radius of the *A*-site ion, namely a larger distortion with a smaller ionic radius in the orthorhombic perovskite lattice. This in turn governs the hybridization between the O 2*p* and M *d* orbitals and hence the effective hopping interaction or one-electron bandwidth of *d* electron. A good example for the filling-control Mott transition is the case of $RNiO_3$ (R being the rare-earth ion) [2]. The $RNiO_3$ is paramagnetic metallic for R = La with a maximal bandwidth, undergoes the thermally induced insulator–metal transition for R = Pr and Nd, and for others are always insulating irrespective of paramagnetic or antiferromagnetic. The filling control can be performed by partly replacing R (*e.g.* La) with alkaline-earth divalent ion (*e.g.* Sr). In conjunction with the bandwidth control, the study of a doping effect on the Mott transition in the form of perovskite lattice enables us to investigate the critical features of the Mott transition in a wide parameter space.

Here we will review the study of the Mott transition in some 3*d* TMO systems with perovskite structure, by exemplifying the cases of $RTiO_3$, RVO_3, $RMnO_3$, and their hole-doped systems. The $RTiO_3$ is a $S = 1/2$ Mott–Hubbard insulator with the band filling $n = 1$ for the Ti 3*d* band (seen Fig. 2). A prototypical mass-enhancement feature, generic for the Mott transition but not like the case of doped cuprates, is observed. The orbital degeneracy in the t_{2g} state should play an important role not only in realizing the A-site specific magnetic state, say the ferromagnetic ground state of $YTiO_3$, but also in the Mott transition process itself. However, this effect has not been made transparent enough as yet perhaps because of large quantum fluctuation of orbital for the $RTiO_3$ family [3]. By contrast, the active role of orbital degree of freedom is more visible for the RVO_3 system that possesses $3d^2$ ($S = 1$) configuration of V^{3+} ions. We show the interplay between the orbital and spin orders in various RVO_3 as well as the strongly anisotropic electronic structure induced by the orbital ordering. The orbital correlation is likely important also in understanding an anomalous nature of the metallic state on the verge of the Mott transition in $La_{1-x}Sr_xVO_3$.

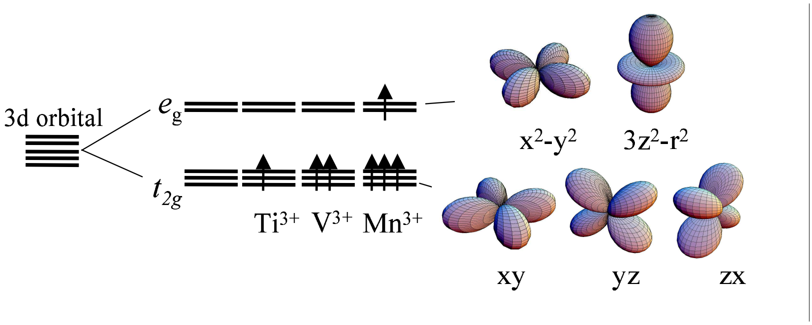

Fig. 2. Crystal-field splitting of five-fold degenerate atomic $3d$ levels into lower t_{2g} (triply degenerate) and higher e_g (doubly degenerate) levels in trivalent Ti, V and Mn ions.

We will also give a brief review on the Mott transition in $La_{1-x}Sr_xMnO_3$ that keeps the ferromagnetic state in the course of the transition. As another example of the metal–insulator transition, the bicritical feature between the charge/orbital ordered state and the ferromagnetic metallic state is described in nearly half-doped manganites. The competition of the ordered phases is closely related to the colossal magnetoresistance effect as well as to unconventional phase-controllability, such as photo-induced insulator-metal transition [4,5] and current switching effect [6], achieved so far in the manganite system.

2. $RTiO_3$

Perovskite-type titanate $RTiO_3$ (where R is a trivalent rare-earth ion or Y) is well known [3, 7–12] as a Mott insulator with $S = 1/2$. One of the advantages in this system is that both of the one-electron bandwidth and the band filling can be controlled [12] by the chemical modification of the R-site. As schematically shown in Fig. 3, the ground state varies from antiferromagnetic to ferromagnetic when the R-ion is changed from La

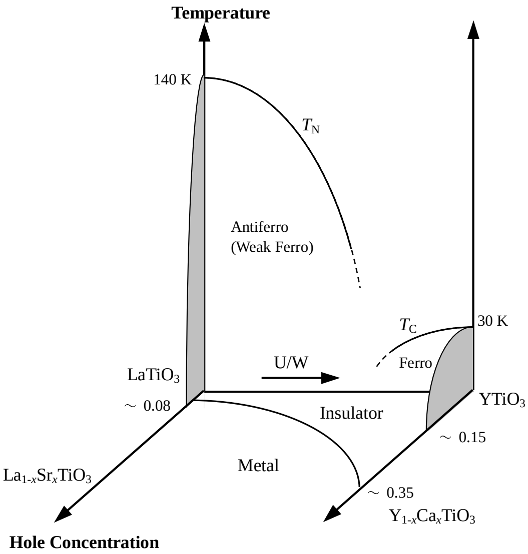

Fig. 3. A schematic phase diagram of $\mathrm{R}_{1-x}A_x\mathrm{TiO}_{3+y/2}$ system, where hole concentration corresponds to $x+y$.

to Y. The Néel temperature and the Curie temperature are about 140 K and 30 K, respectively. The filling-control can be achieved by partially substituting La or Y site with divalent Sr or Ca ion, and/or by introducing excess oxygen. In $\mathrm{LaTiO_3}$, both the antiferromagnetic phase and insulating phase are destroyed by the hole-doping of less than 0.1 [13]. By contrast, the metallic phase is obtained by the hole-doping as much as ≈ 0.35 in the case of $\mathrm{YTiO_3}$ although the ferromagnetic phase disappears at much less doping concentration (< 0.2) [9]. The different doping-level needed for the insulator-metal transition is ascribed to the different correlation strength of the respective parent compound, that is manifested by the difference in the Mott–Hubbard gap (ca. 0.2 eV and 0.8 eV for $\mathrm{LaTiO_3}$ and $\mathrm{YTiO_3}$, respectively) [14]. In the sufficiently hole-doped metallic phases of the both compounds, several hallmarks that are characteristic of Fermi liquid, such as T-squared resistivity, T-independent susceptibility, and T-linear electronic specific heat, T-independent Hall coefficient, are observed [15, 16].

As displayed in Fig. 4(b), the inverse of Hall coefficient in the metallic phases shows almost linear dependence on the band filling ($= 1 - x$, where x denotes the Sr- or Ca-concentration or the hole doping level) [15]. The straight line in the figure is the expected dependence for a simple parabolic band. Therefore, the experimental result suggests that the Fermi surface area is expanded with the filling as expected for a free-electron like band. In Fig. 4(a), the electronic specific heat coefficient γ and the Pauli-like sus-

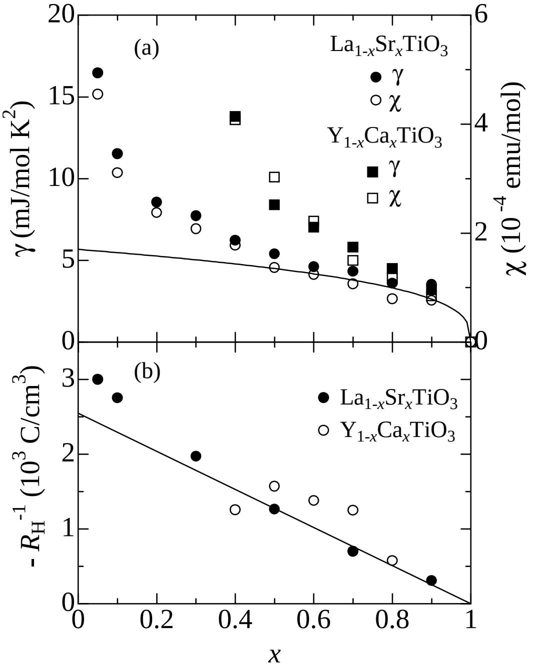

Fig. 4. x dependence of (a) the electronic specific heat coefficient γ and Pauli-like susceptibility χ and (b) the inverse of the Hall coefficient for $La_{1-x}Sr_xTiO_3$ and $Y_{1-x}Ca_xTiO_3$.

ceptibility χ are plotted against x. In a simple free-electron model with a constant effective mass, both quantities should be proportional to $(1-x)^{1/3}$ as represented by a solid line in the figure. In contrast to the case of Hall coefficient, they clearly show significant deviation from the expected behavior and steep increase as the insulator–metal phase boundary is approached. This indicates a critical mass-enhancement [15] of the electron-type charge carriers and is in accord with the Brinkman–Rice picture [17].

Although the overall behavior is clarified as described above, the critical region near the metal–insulator transition point and the antiferromagnetic instability point should be examined in more detail. To control the electron filling more finely, the hole doping by introducing excess oxygen has been attempted [13]. The resistivity of several oxygen-doped crystals are displayed in Fig. 5. The sample with $\delta \approx 0.06$ shows a gentle upturn at around 90 K, slightly below Néel temperature (see Fig. 6(a)), but the resistivity remains finite even at the lowest temperature. Therefore, the ground state of this sample is an antiferromagnetic metal. The crystal with $\delta \approx 0.08$ locates at the antiferromagnetic instability point, and the low-temperature resistiv-

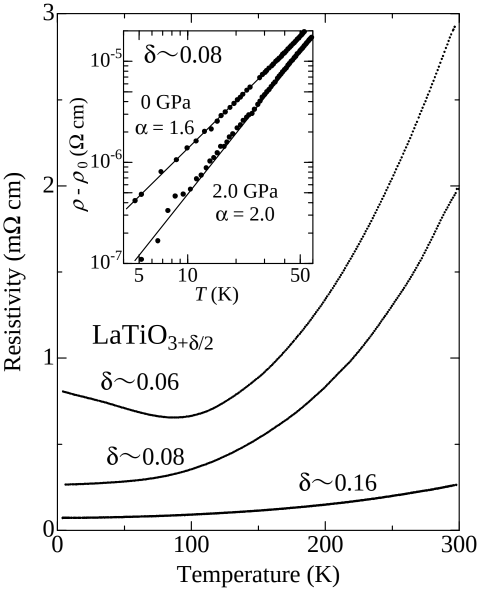

Fig. 5. Temperature dependence of resistivity for the metallic samples with excess oxygen $LaTiO_{3+y/2}$. The inset exemplifies T^{α}-type dependence of the resistivity for $\delta \approx 0.08$ below 60 K at ambient pressure and 2.0 GPa. The straight lines correspond to $\alpha = 1.6$ and 2.0 dependencies, respectively.

ity exhibits T^{α}-type behavior with $\alpha = 1.6$, as exemplified in the inset to Fig. 5. This value is distinct from the value (=2) expected for the Fermi liquid, and is close to 1.5 that is predicted by the self-consistent renormalization theory [18] for the compound at the antiferromagnetic instability point. Application of pressure of 2.0 GPa changes the exponent to $\alpha = 2$, as shown in the inset. Applied pressure enhances the one-electron bandwidth, therefore the electron system is driven away from the antiferromagnetic instability point and restores the Fermi liquid behavior.

In Fig. 6, several important quantities are plotted as a function of hole doping level [13]. The Néel temperature decreases with increasing hole-doping, and disappears at $\delta_c^{\mathrm{mag}} \approx 0.08$, as shown in the panel (a). The inverse of Hall coefficient at 2 K is plotted in the panel (b). The decrease of this quantity for $\delta \approx 0.06$ sample compared with $\delta \approx 0.08$ sample is accounted for in terms of reduced Fermi surface area due to the opening of spin density wave gap. The removal of a part of the Fermi surface causes the reduction of the density of states at the Fermi surface. This manifests itself as the decrease of the electronic specific heat coefficient γ in the antiferromagnetic metallic phase, as shown in the panel (c). Therefore, the filling-control metal–insulator transition in this system is summarized as follows: As the

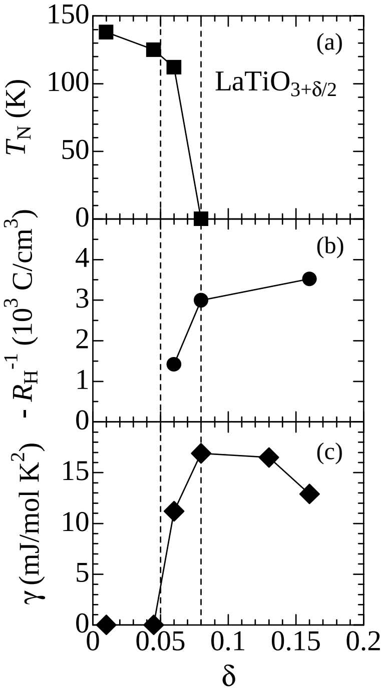

Fig. 6. Hole doping dependence of (a) Néel temperature, (b) inverse of Hall coefficient, and (c) electronic specific heat coefficient. Vertical dashed lines indicate the insulator-metal ($\delta_c^{IM} \approx 0.05$) and antiferromagnetic-paramagnetic ($\delta_c^{mag} \approx 0.08$) phase boundaries.

metal–insulator transition point is approached from the metallic side, the effective mass of the charge carriers is critically enhanced due to the filling-dependent correlation effect. Once the antiferromagnetic ordering sets in, some portion of the Fermi surface is gapped, and both the carrier density and the density of states at the Fermi level are reduced. Further increase of band filling toward integer filling eventually drives the system into the Mott insulating state.

3. RVO$_3$

Perovskite-type $La_{1-x}Sr_xVO_3$ is a classic Mott transition system [1, 19]. The parent compound $LaVO_3$ and related materials RVO_3, where R is a trivalent rear-earth ion or Y, are Mott–Hubbard type insulators with the electron configuration of $3d^2$. Besides the manganites, these vanadates have been attracting current interest because of ordering and fluctuation of orbital degrees of freedom [20–26]. RVO_3 undergoes not only a magnetic transition to an antiferromagnetic (AF) state but also a structural phase transition coupled with orbital ordering as temperature is decreased. These compounds exhibit a variety of spin and orbital ordered states depending on the rare-earth site ions [22,25,27,28]. Figure 7(a) presents a schematic phase diagram of spin and orbital ordering (SO and OO) in this system [29]. Between $\mathrm{PrVO_3}$ and $\mathrm{LuVO_3}$, the structural phase transition perhaps accompanied by the OO with an alternative $d_{xy}^1 d_{yz}^1 / d_{xy}^1 d_{zx}^1$ electron configuration (Fig. 7(c)) takes place above the transition temperature of C-type antiferromagnetism (T_{SO1}) [21]. Here, we call this OO G-type by analogy to spin ordering. By contrast, $\mathrm{LaVO_3}$ and $\mathrm{CeVO_3}$ undergo the structural phase transition at a few degrees below T_{SO1}, suggesting that the C-type SO induces the G-type OO and related structural phase transition [30]. In the R = Dy to Lu compounds, on the other hand, the pattern of the SO turns into G-type, and the OO does into C-type concomitantly below the second structural and magnetic transition temperatures ($T_{\mathrm{OO2}} = T_{\mathrm{SO2}}$).

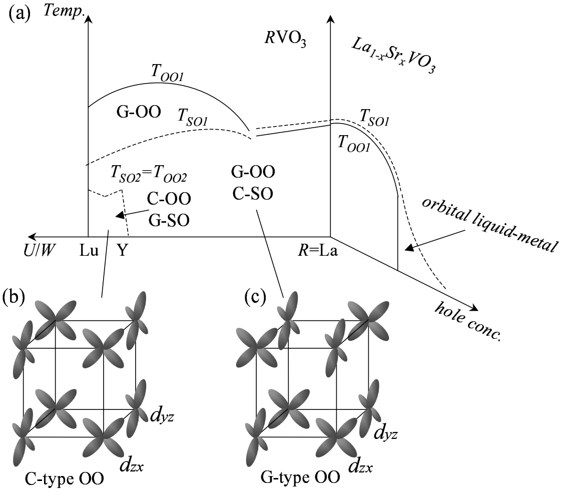

Fig. 7. (a) Schematic phase diagrams of $\mathrm{RVO_3}$ and $\mathrm{La_{1-x}Sr_xVO_3}$. The abbreviations mean G-type (G), C-type (C), spin and orbital ordering (SO and OO). (b), (c) Schematic structures of the C-type and G-type OO in the perovskite-type $\mathrm{RVO_3}$. Gray lobes indicate occupied d_{yz} and d_{zx} orbitals on the vanadium ions. The commonly occupied d_{xy} orbitals are displaced for clarity.

These SO and OO are expected to cause appreciable anisotropy in the electronic structure and charge dynamics through the spin-charge-orbital correlations. Figures 8(a) and (b) present optical conductivity ($\sigma(\omega)$) spectra for $\boldsymbol{E} \parallel c$ and $\boldsymbol{E} \perp c$ at 10 K in $\mathrm{LaVO_3}$ and $\mathrm{YVO_3}$, which have different types of SO and OO. The 2 eV band in the $\sigma(\omega)$ spectrum has been assigned to the Mott–Hubbard gap transition [31–34]. At 10 K, the peak around 2 eV in the $\boldsymbol{E} \parallel c$ spectra shows distinct shape and high intensity, which has seldom been observed in other Mott–Hubbard insulators in three-dimension [31,35]. Such an anisotropic and distinct spectral feature for the Mott–Hubbard gap transition reflects the anisotropic electronic structure due to the SO and OO with one-dimensional character, as argued in the following.

As seen in Figs. 8(a) and (b), the 2 eV band in the $\sigma(\omega)$ for $\boldsymbol{E} \parallel c$ is composed of two peaks. At the ground state (10 K), the lower-lying peak 1 bears much larger (smaller) intensity than the higher-lying peak 2 in $LaVO_3$ (YVO_3), as clearly seen in the spectral decomposition (broken lines). In the both vanadates, an electron can hop only between the d_{yz} orbitals or d_{zx} ones on the neighboring V site along the c-axis through the π-bonding with the O

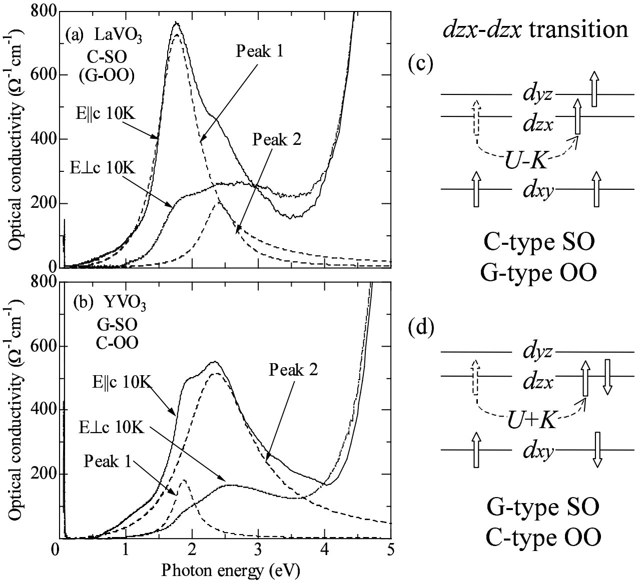

Fig. 8. Optical conductivity spectra for $\boldsymbol{E} \parallel c$ and $\boldsymbol{E} \perp c$ (solid lines) in single crystals of (a) $LaVO_3$ and (b) YVO_3 at 10 K. Broken lines indicate the fitting result with the Lorentz model for the c-axis polarized optical conductivity spectrum in both compounds. The lower- and higher-lying peaks are the Mott–Hubbard gap transitions, denoted "peak 1" and "peak 2", respectively. (c), (d) Change of t_{2g} orbital states on the neighboring V sites along the c-axis in the optical d_{zx}-d_{zx} transition in each type of SO and OO.

$2p_y$ or $2p_x$ state. The d_{yz}-d_{yz} transition energy should be nearly equal to the d_{zx}-d_{zx} one. In Figs. 8(c) and (d), we exemplify the change of the t_{2g} orbital states on the neighboring V sites along the c-axis in the optical excitation between the d_{zx} orbitals in the respective case of SO and OO. The energy of the d_{zx}-d_{zx} excitation in the C-type SO and G-type OO is smaller than that in the G-type SO and C-type OO by an energy of the effective Hund's-rule coupling. Therefore, the $\sigma(\omega)$ spectrum for $\boldsymbol{E} \parallel c$ has a peak with a large intensity at $U'-K$ for the C-type SO and G-type OO, or otherwise at $U'+K$ for the G-type SO and C-type OO, where U' and K denote the energy of effective on-site Coulomb repulsion and Hund's-rule coupling, respectively. Such orbital-dependent Mott–Hubbard gap transitions and their selection rules in the spin- and orbital-ordered state can roughly explain spectral features in the respective ground-states of $LaVO_3$ and YVO_3.

In RVO_3, the hole doping by substitution of R with Sr or Ca causes a transition from a correlated insulator to a metal and the AF spin long-range order gradually disappears with the increase of doping level. The critical

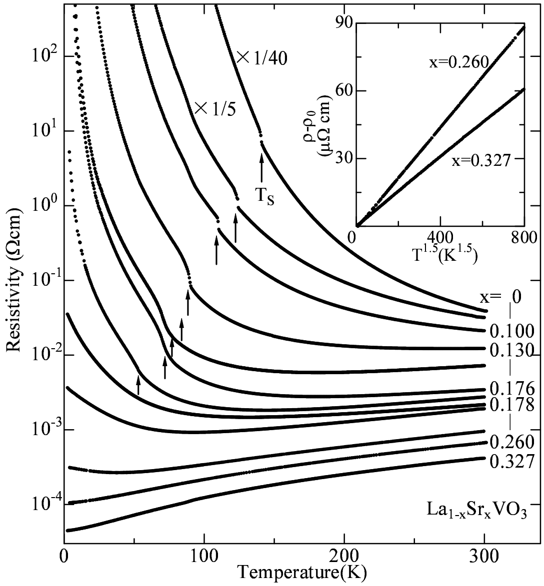

Fig. 9. Temperature (T) dependent resistivity for single crystals of $La_{1-x}Sr_xVO_3$. The resistivity curve for $x \leq 0.176$ shows a kink corresponding to the occurrence of the structural phase transition due to the G-type orbital ordering. Arrows indicate the structural phase transition temperature (T_{OO1}). The inset shows a plot of $\rho-\rho_0$ *vs.* $T^{1.5}$ for $x = 0.327$ in the PM metal phase and $x = 0.260$ in the AF metal phase, where ρ and ρ_0 are resistivity and residual resistivity, respectively.

behavior of the metal–insulator transition (MIT) has recently been investigated by using high-quality single crystals of $La_{1-x}Sr_xVO_3$ [23]. We display the temperature dependence of the resistivity for samples with several doping levels x in Fig. 9. The resistivity for $x \leq 0.176$ shows an insulating behavior and has a kink indicated by an arrow which signals the occurrence of the first order phase transition. This phase change corresponds to a lattice-structural transition from an orthorhombic to a monoclinic form [30], that is associated by the G-type orbital ordering. With the increase of x, the structural phase transition temperature (T_{OO1}) systematically decreases and eventually the transition disappears around $x = 0.178$. In the critical region of MIT ($0.178 \leq x \leq 0.210$), the resistivity shows upturn at a low temperature, while that for $x = 0.260$ and 0.327 monotonously decreases in the whole temperature region down to 2 K. The extrapolated zero-temperature conductivity remains finite for $0.178 \leq x \leq 0.210$, while zero for $x \leq 0.176$. The intrinsic MIT at zero temperature occurs around $x = 0.176$, accompanied by the onset of the structural phase transition, *i.e.*, the orbital order-disorder transition.

As shown in the phase diagram (Figs. 7 and 10(a)), T_{SO1} and T_{OO1} systematically decrease with the increase of x. The temperature interval between them is almost unchanged, suggesting that the C-type SO induces the orbital ordering and the related structural phase transition in the Sr-doped compounds as well as in $LaVO_3$ and $CeVO_3$. In $La_{1-x}Sr_xVO_3$, this AF ordering remains until $x = 0.260$ and the ground state becomes the AF metal, while the first-order structural phase transition disappears concomitantly with the MIT around $x = 0.178$. In this system, therefore, the boundary of the structural phase transition is different from that between the paramagnetic (PM) and AF phase. In other words, the ground state of this system perhaps undergoes the transition from the orbital ordered AF insulator to the orbital disordered AF metal with the increase of the Sr concentration x, and eventually becomes the orbital disordered PM metal.

Thermal and transport properties in $La_{1-x}Sr_xVO_3$ show distinct features between the PM and the AF metal phases. The PM metal phase ($x > 0.260$) can be characterized by filling-dependent mass renormalization. The electronic specific heat coefficient γ is plotted against x in Fig. 10(c). With decreasing the doping level from $x = 0.327$ to 0.260, γ is enhanced, reflecting the mass renormalization effect in the vicinity of the Mott transition [17]. The magnitude of γ for $x = 0.260$ is $59\mathrm{mJ/K^2mol}$ and approximately seven times as large as that of the end member $SrVO_3$, reported previously [36]. Moreover, the value per transition-metal atom is even larger than that of other Mott transition systems [13, 37], *e.g.* $\gamma \simeq 40\mathrm{mJ/K^2V}$-atom for $V_{2-y}O_3$[3]. In the AF metal phase ($0.178 \leq x \leq 0.260$), however, γ rather decreases with the decrease of x toward the MIT. In the Fermi-liquid

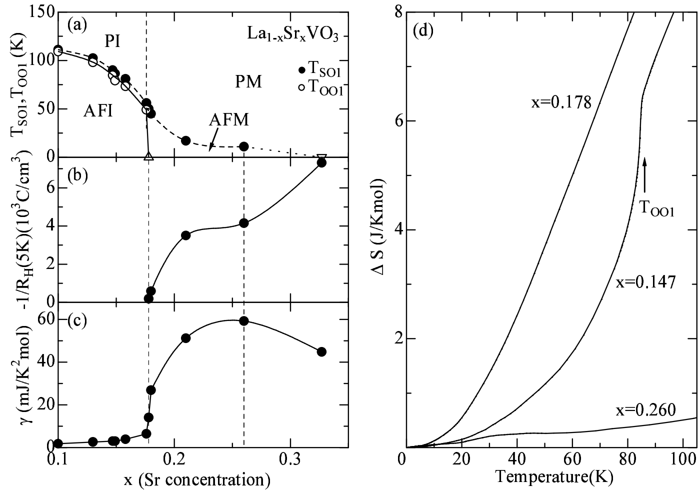

Fig. 10. (a): The electronic phase diagram of $La_{1-x}Sr_xVO_3$. (b), (c): The Sr concentration (x) dependence of (b) the inverse of the Hall coefficient R_H at 5 K and (c) the electronic specific heat coefficient γ. (d): T dependence of entropy related to the structural phase transition, ΔS, for the insulating sample ($x = 0.147$), the sample ($x = 0.178$) on the verge of the metal–insulator trasition, and the metallic sample ($x = 0.260$) of $La_{1-x}Sr_xVO_3$ are plotted. An arrow indicates the temperature of the structural phase transition (T_{OO1}).

picture, except for the region very close to the AF/PM phase boundary, the low temperature resistivity in the PM metal phase is predicted to show T^2-dependence, and the T^2-term coefficient A and the γ obey the Kadowaki–Woods relationship, $A = \alpha\gamma^2$ with $\alpha \simeq 1 \times 10^{-11}\Omega\mathrm{cm}/(\mathrm{mJ/K^2mol})^2$ [15, 37, 38]. As seen from the inset of Fig. 9, however, the resistivity for the $x = 0.327$ PM metallic sample is still in proportion to $T^{1.5}$, which suggests the strong AF spin fluctuation extending over a broad x-region beyond the AF/PM critical point [39].

We show the x-dependence of inverse of the Hall coefficient at 5 K in Fig. 10(b). The Hall coefficient for all the metallic crystals is negative in sign. In the PM metal phase, Hall coefficient is almost independent of temperature, with the magnitude of approximately $2\times10^{-4}\mathrm{cm^3/C}$. This is consistent with the picture of a large Fermi surface containing a few carrier electrons per vanadium atom. In the AF metal phase, by contrast, the magnitude of Hall coefficient shows a rapid increase at low temperatures below T_{SO1}. At $x = 0.178$, the lowest temperature Hall coefficient is as large as $-5 \times 10^{-3}\mathrm{cm^3/C}$. The result indicates that in the AF metal phase the carrier number decreases with approaching the insulating phase, perhaps due to the occurrence of the SDW-like gap in the k-space. The reduction in the carrier density is roughly consistent with the decrease of γ, which indicates the shrinkage of the Fermi surface in the AF metal phase, while keeping or enhancing the mass renormalization effect.

The observed anomalous behavior of the entropy also seems to indicate the correlation of orbital ordering around the MIT. We define $\Delta C = (C(x)-\gamma(x)T)-(C(x=0.327)-\gamma(x=0.327)T)$ as the specific heat related to the structure phase transition. Here, we used the phonon term of the specific heat for the $x = 0.327$ PM metal sample $(C(x = 0.327)-\gamma(x = 0.327)T)$ as a reference. Moreover, the specific heat around MIT shows no jump at T_{SO1}, indicating that the contribution of the magnetic transition to ΔC is negligible near the MIT. We plotted the temperature dependence of entropy $\Delta S(T) = \int_0^T \Delta C(T')/T'dT'$ for the samples with several doping levels x in Fig. 10(d). ΔS for the insulating sample ($x = 0.147$) at T_{OO1} is approximately 6.5J/Kmol. Given the transition from the triply degenerated t_{2g} orbitals randomly occupied by two electrons to the G-type orbital ordering, the entropy change is described as $\Delta S = \mathrm{R}\ln 3\times(1-x)$. The present result is roughly consistent with the value. With the increase of x, the jump of the specific heat fades out and ΔS at T_{OO1} decreases. At low temperatures, however, ΔS is rather enhanced near the MIT (see the curve for $x = 0.178$), which suggests the existence of the orbital fluctuation or the related softening of the phonon. Namely, the AF metal phase close to the metal–insulator critical point appears to be crucially affected by strong orbital correlations. With further doping (*e.g.*, in the PM metal phase) the related entropy at low temperatures are fully suppressed, as seen in Fig. 10(d).

4. RMnO$_3$

To overview complex electronic phases induced by a close interplay among the spin, charge, and orbital degree of freedom in the perovskite manganites, we first show in Fig. 11 the electronic phase diagram for $\mathrm{Nd}_{1-x}\mathrm{Sr}_x\mathrm{MnO}_3$ [40, 41]. The end Mott insulator NdMnO$_3$ shows, like LaMnO$_3$, the $3x^2-r^2$ /$3y^2-r^2$ orbital ordered sate. The ferromagnetic interaction within the plane is mediated by the super-exchange interaction in the orbital alternatively-ordered state, and the ferromagnetic Mn-O sheets stack antiferromagnetically along the c axis (A-type antiferromagnetism) via the antiferromagnetic super-exchange interaction. With doping holes via the Sr substitution, the orbital undergoes the disordering (quantum-melting) transition, giving rise to the isotropic ferromagnetic state mediated by the double-exchange interaction. Up to x∼0.4 the kinetic energy of doped holes increases with x, or equivalently the Curie temperature T_{C} increases with x.

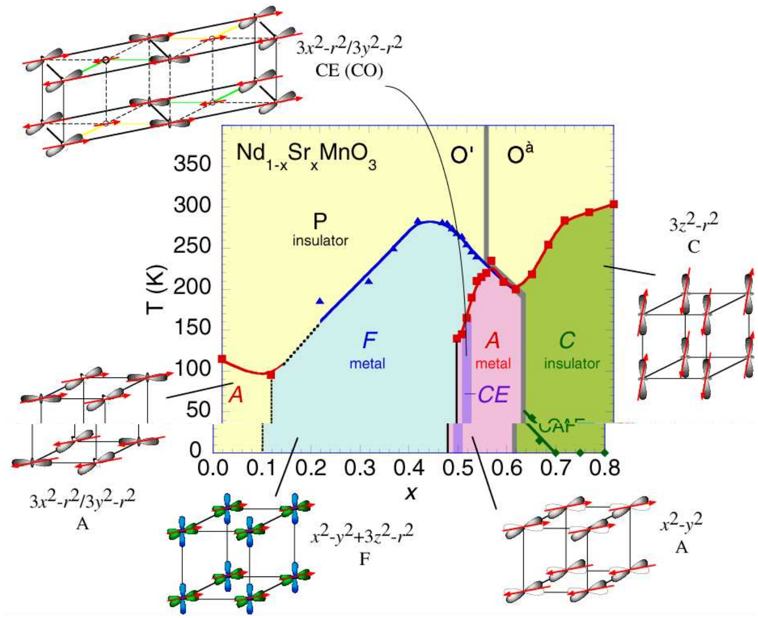

Fig. 11. Electronic phase diagram of $\mathrm{Nd}_{1-x}\mathrm{Sr}_x\mathrm{MnO}_3$ crystal. The abbreviations mean paramagnetic (P), ferromagnetic (F) *CE*-type antiferromagnetic and charge-ordered (CE), *A*-type antiferromagnetic (A), *C*-type antiferromagnetic (C). O′ and $\mathrm{O}^{\grave{a}}$ indicate the orthorhombic lattice structures with $a \approx b > c$ and $a \approx b < c$, respectively.

With further hole doping, in particular exceeding $x = 0.5$, the double-exchange interaction of e_g electron and the super-exchange interaction between the t_{2g} local spins can find the compromise to realize the low-dimensional ferromagnetic structures at the ground state. Namely, at 0.52< x <0.62 the ground state is *A*-type antiferromagnetic associated with the *ferro*-orbital order of $x^2 - y^2$ [42, 43]. The fully-spin polarized $x^2 - y^2$ band is 2-dimensional (2D) in nature and nearly half-filled. The in-plane ferromagnetic state is mediated by the double-exchange interaction in the $x^2 - y^2$ orbital ordered state, while along the c-axis the free energy is gained by the antiferromagnetic coupling. In fact, the resistivity for $x = 0.55$ show the 2D metallic feature in spite of nearly cubic lattice structure [44]. Thus, albeit similarly *A*-type antiferromagnetic, the 2D double-exchange sheets realized in the over-doped region of the manganites is distinct from the $3x^2 - r^2/3y^2 - r^2$ Mott-insulating state for $x = 0$.

With further increasing the doping level x above 0.62, the kinetic energy of carriers is further decreased (this should be viewed as the decrease of e_g electron filling rather than as the increase of hole count), and the double-exchange path is restricted along the c-axis chain. Namely, the ferromagnetic chain along the c-axis is coupled antiferromagnetically (C-type). This state is mediated by the $ferro$-ordering of $3z^2-r^2$ orbitals. In this case, the c-axis charge response is no more metallic, perhaps due to the strong charge correlation inherent to the 1D system. Such an orbital ordering appear to persist up to as high a temperature as 600–700 K, far above the spin ordering (Néel) temperature(200–280 K). In ordering the orbitals, the electronic structure becomes highly anisotropic as probed by the polarized optical conductivity spectra [45].

Now, let us turn our eyes to the low-doping critical region for the insulator–metal transition. In Fig. 12 is summarized the doping(x)-dependence of Curie temperaure, Hall coefficient, and electronic specific heat constant γ in the vicinity of metal–insulator (MI) transition ($x_\mathrm{c} = 0.16$) of $\mathrm{La}_{1-x}\mathrm{Sr}_x\mathrm{MnO}_3$ [46]. The hatched region represents the MI transitional region where the resistivity shows up-turn in lowering temperature below T_c, where some ordering in charge and/or orbital sectors is likely to occur [47]. The Hall coefficient, that contains no component of anomalous Hall effect in such a low temperature region, takes a positive small value over the whole metallic region ($x >$0.18), indicating nominally ∼1 hole per Mn site. This is characteristic of large Fermi surface of the fully spin-polarized band. In other words, the Fermi surface retains its area down to near the metal–insulator phase boundary.

The γ value shows a minimal enhancement even near the MI boundary and steeply decreases to zero in the transitional region in between $x = 0.18$ and 0.15. This is in sharp contrast with the canonical cases of the doping-induced Mott transition, as already described in the present paper for the cases of doped LaTiO_3 and LaVO_3, in which the critical enhancement of γ or the strong mass renormalization effect is observed.

The diffuse charge dynamics in the ferromagnetic metallic phase close to the MI point manifests itself in the optical conductivity spectra at the ground state. The low-energy spectral weight (Drude weight) is steeply decreased as the compound approaches the MI transitional boundary from the high-x side [48]. Some lattice anomaly is also discerned in the anomalous x-dependence of Debye temperature. The doping-induced metallic ground state in $\mathrm{La}_{1-x}\mathrm{Sr}_x\mathrm{MnO}_3$ is fully spin-polarized (half-metallic) with no spin degree of freedom left at zero temperature. The suppression of the Drude weight cannot be interpreted in terms of a small Jahn–Teller polaron picture, since no appreciable mass renormalization is observed. The strong scattering in such a fully spin-polarized ground sate may be ascribed to the orbital

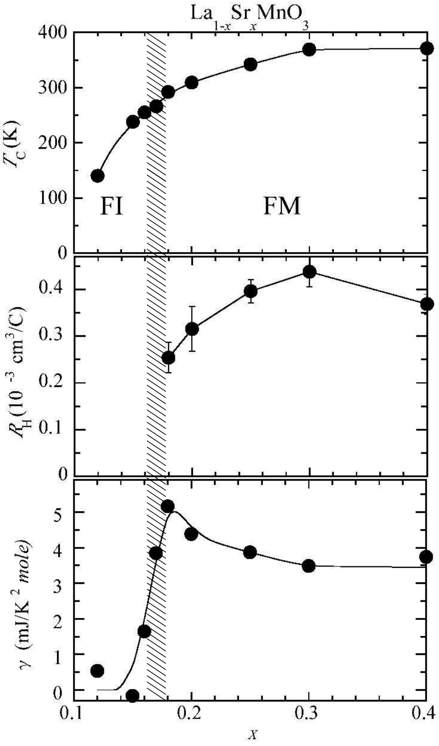

Fig. 12. Doping level (x) dependence of Curie temperature (T_{C}), Hall coefficient R_{H} and electronic specific heat coefficient γ for $\mathrm{La}_{1-x}\mathrm{Sr}_x\mathrm{MnO}_3$. FI and FM indicate ferromagnetic insulator and metal. An area for $0.16 \leq x \leq 0.18$ indicate the metal–insulator transitional region.

degree of freedom in the e_g state, as thoretically argued [49, 50], or otherwise to dynamical phase segregation [50] composed of the ferromagnetic-metallic (double-exchange-mediated) and ferromagnetic-insulating (orbital-ordered super-exchange-mediated) states. The puzzling nature of the Mott transition is still left to be elucidated.

As another example of notable metal–insulator phenomena in manganites, we show in Fig. 13 the bicritical features as a consequence of competition of the two phases, *i.e.*, the ferromagnetic-metal state and the charge /orbital ordered state. Such a competition occurs in a broad range of perovskite-related manganites with hole-doping levels around $x = 0.5$ [41]. The case shown in Fig. 13 is for the $x = 0.45$ manganites, $\mathrm{Pr}_{0.55}(\mathrm{Ca}_{1-y}\mathrm{Sr}_y)_{0.45}\mathrm{MnO}_3$, with controlled bandwidth via the alkaline-earth compostion y. As seen in the inset, the resistivity for y <0.25 shows a sharp up-turn followed by an insulating behavior at the charge-orbital ordering temperature T_{CO}. (The charge/orbital ordering pattern is the so-called CE-type as illustrated in Fig. 11 for the $x = 0.50$ ground state of $\mathrm{Nd}_{1-x}\mathrm{Sr}_x\mathrm{MnO}_3$.) For y >0.25 with the increased bandwidth, the compound shows the ferromagnetic transition at T_{C} accompanied by the decrease of resisitivity. The important feature to be noted is that the both transition temperatures, T_{CO} and T_{C}, decrease towards to the biciritical point $y = 0.25$ from the both sides to coincide with each other. (See also the resistivity curves (the inset of Fig. 13) for $y = 0.2$ and $y = 0.25$ whose up-turn and down-turn occur at the nearly identical temperature, namely $T_{\mathrm{C}} \sim T_{\mathrm{CO}}$.)

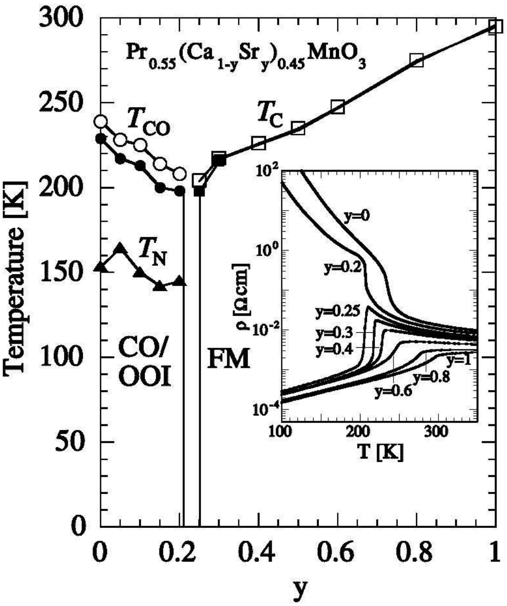

Fig. 13. Phase diagram of $\mathrm{Pr}_{0.55}(\mathrm{Ca}_{1-y}\mathrm{Sr}_y)_{0.45}\mathrm{MnO}_3$. The inset shows temperature dependent resistivity for samples with several Sr concentration y.

The colossal magnetoresistance (CMR) usually occurs around such a bicritical point between the competing phases. The charge/orbital ordered phase near the biciritical point is amenable to a relatively low external magnetic field and turned into an orbital (quantum-)disordered ferromagnetic state, accompanying the conspicuous insulator-metal transition [41]. On the other hand, the compound in the ferromagnetic side near the bicritical point shows a prototypical CMR behavior. In fact, the variation of the T-dependent resistivity curve with increasing y (see the inset of Fig. 13) quite resembles that of the $y = 0.25$ curve with increasing an applied magnetic field.

The bicritical point and the phase behaviors around it are quite sensitive to the randomness of the system. Other choice of the perovskite *A*-site ions, say *R* and Sr/Ba, while keeping the averaged ionic radius or the effective one-electron bandwidth constant, gives rise to much a reduced T_{C} and resultantly a further enhanced CMR effect. This is highly nontrivial, since the quenched disorder or some frustration arising from the *A*-site ions causes even enhanced phase fluctuation with suppressed long-range order. Too strong disorder, such as the impurity (*e.g.* Cr)-doping on the Mn site [51, 52] or the lattice strain inherent to the ceramics grain boundaries [53], seems to cause the phase separation on various length-scale and time-scale (relaxor-like bhaviors) in such a bicritical region. This is also a source of CMR via percolation mechanism.

We would like to thank Y. Tomioka, T. Okuda, and H. Kuwahara for their help in preparing the manuscript.

REFERENCES

[1] M. Imada, A. Fujimori, Y. Tokura, *Rev. Mod. Phys.* **70**, 1039 (1998).

[2] J.B. Torrance, P. Lacorre, A.I. Nazzal, E.J. Ansaldo, Ch. Niedermayer, *Phys. Rev.* **B45**, 8209 (1992).

[3] B. Keimer, D. Case, A. Ivanov, J.W. Lynn, M. v. Zimmermann, J.P. Hill, D. Gibbs, Y. Tagchi, Y. Tokura, *Phys. Rev. Lett.* **85**, 3946 (2000).

[4] M. Fiebig, K. Miyano, Y. Tomioka, Y.Tokura, *Science* **280**, 1925 (1998).

[5] V. Kiryukhin, D. Casa, J.P. Hill, B. Keimer, A. Vigliante, Y. Tomioka, Y. Tokura, *Nature* **386**, 813 (1997).

[6] A. Asamitsu, Y. Moritomo, Y. Tomioka, T. Arima, Y. Tokura, *Nature* **373**, 407 (1995).

[7] D.A. MacLean, Hok-Nam Ng, J.E. Greedan, *J. Solid State Chem.* **30**, 35 (1979).

[8] F. Lichtenberg, D. Widmer, J.G. Bednorz, T. Williams, A. Reller, *Z. Phys.* **B82**, 211(1991).

[9] Y. Taguchi, Y. Tokura, T. Arima, F. Inaba, *Phys. Rev.* **B48**, 511 (1993).

[10] Y. Okada, T. Arima, Y. Tokura, C. Murayama, N. Môri, *Phys. Rev.* **B48**, 9677(1993).

[11] D.A. Crandles, T. Timusk, J.D. Garrett, J.E. Greedan, *Phys. Rev.* **B49**, 16207 (1994).

[12] T. Katsufuji, Y. Taguchi, Y. Tokura, *Phys. Rev.* **B56**, 10145 (1997).

[13] Y. Taguchi, T. Okuda, M. Ohashi, C. Murayama, N. Môri, Y. Iye, Y. Tokura, *Phys. Rev.* **B59**, 7917 (1999).

[14] T. Katsufuji, Y. Okimoto, Y. Tokura, *Phys. Rev. Lett.* **75**, 3497 (1995).

[15] Y. Tokura, Y. Taguchi, Y. Okada, Y. Fujishima, T. Arima, K. Kumagai, Y. Iye, *Phys. Rev. Lett.* **70**, 2126 (1993).

[16] K. Kumagai, T. Suzuki, Y. Taguchi, Y. Okada, Y. Fujishima, Y. Tokura, *Phys. Rev.* **B48**, 7636 (1993).

[17] W.F. Brinkman, T. M. Rice, *Phys. Rev.* **B2**, 4302 (1970).

[18] K. Ueda, *J. Phys. Soc. Jpn.* **43**, 1497 (1977).

[19] N.F. Mott, *Metal-Insulator Transitions* Taylor and Francis, London 1990.

[20] For a review, *Colossal Magnetoresistive Oxides*, ed. Y. Tokura, Gordon & Breach Science Publishers, 2000.

[21] H. Sawada, N. Hamada, K. Terakura, T. Asada, *Phys. Rev.* **B53**, 12742 (1996).

[22] M. Noguchi, A. Nakazawa, S. Oka, T. Arima, Y. Wakabayashi, H. Nakao, Y. Murakami, *Phys. Rev.* **B62**, R9271 (2000).

[23] S. Miyasaka, T. Okuda, Y. Tokura, *Phys. Rev. Lett.* **85**, 5388 (2000).

[24] G. Khaliullin, P. Horsch, A.M. Oleś, *Phys. Rev. Lett.* **86**, 3879 (2001).

[25] G.R. Blake, T.T.M. Palstra, Y. Ren, A.A. Nugroho, A.A. Menovsky, *Phys. Rev. Lett.* **87**, 245501 (2001).

[26] S. Miyasaka, Y. Okimoto, Y. Tokura, *J. Phys. Soc. Jpn.* **71**, 2086 (2002).

[27] V.G. Zubkov, G.V. Bazuev, V.A. Perelyaev, G.P. Shveikin, *Sov. Phys. Solid State* **15**, 1079 (1973).

[28] H. Kawano, H. Yoshizawa, Y. Ueda, *J. Phys. Soc. Jpn.* **63**, 2857 (1994).

[29] S. Miyasaka, *et al.*, unpublished.

[30] P. Bordet, C. Chaillout, M. Marezio, Q. Haung, A. Santoro, S.-W. Cheong, H. Takagi, C.S. Oglesby, B. Batlogg, *J. Solid State Chem.* **106**, 253 (1993).

[31] T. Arima, Y. Tokura, J.B. Torrance, *Phys. Rev.* **B48**, 17006 (1993).

[32] F. Inaba, T. Arima, T. Ishikawa, T. Katsufuji, Y. Tokura, *Phys. Rev.* **B52**, 2221 (1995).

[33] M. Kasuya, Y. Tokura, T. Arima, H. Eisaki, S. Uchida, *Phys. Rev.* **B47**, 6197 (1993).

[34] K. Maiti, D.D. Sarma, *Phys. Rev.* **B61**, 2525 (2000).

[35] G. A. Thomas, D.H. Rapkine, S.A. Cater, *Phys. Rev. Lett.* **73**, 1529 (1994).

[36] I.H. Inoue, O. Goto, H. Makino, N. E. Hussey, M. Ishikawa, *Phys. Rev.* **B58**, 4372 (1998).

[37] S. Miyasaka, H. Takagi, Y. Sekine, H. Takahashi, N. Mori, R.J. Cava, *J. Phys. Soc. Jpn.* **69**, 3166 (2000).

[38] K. Kadowaki, S.B. Wood, *Solid State Commun.* **58**, 507 (1986).

[39] T. Moriya, *Spin Fluctuation in the Itinerant Electron Magnetism*, Springer, Berlin 1985.

[40] H. Kuwahara, Y. Moritomo, Y. Tomioka, A. Asamitsu, M. Kasai, R. Kumai, Y. Tokura, *Phys. Rev.* **B56**, 9386 (1997).

[41] Y. Tokura, Y. Tomioka, *J. Mag. Mag. Matter.* **200**, 1 (1999).

[42] R. Maezono, S. Ishihara, N. Nagaosa, *Phys. Rev.* **B58**, 11583 (1998).

[43] H. Kawano, R. Kazimoto, H. Yoshizawa, Y. Tomioka, H. Kuwahara, Y. Tokura, *Phys. Rev. Lett.* **78**, 4253 (1997).

[44] H. Kuwahara, T. Okuda, Y. Tomioka, A. Asamitsu, Y. Tokura, *Phys. Rev. Lett.* **82**, 4316 (1999).

[45] K. Tobe, T. Kimura, Y. Tokura, unpublished.

[46] T. Okuda, A. Asamitsu, Y. Tomioka, T. Kimura, Y. Taguchi, Y. Tokura, *Phys. Rev. Lett.* **81**, 3203 (1998).

[47] Y. Endoh, K. Hirota, S. Ishihara, S. Okamoto, Y. Murakami, A. Nishizawa, T. Fukuda, H. Kimura, H. Nojiri, K. Kaneko, S. Maekawa, *Phys. Rev. Lett.* **82**, 4328 (1999).

[48] E. Saitoh, Y. Tomioka, T. Kimura, Y. Tokura, *J. Phys. Soc. Jpn.* **69**, 2403 (2000).

[49] S. Ishihara, M. Yamanaka, N. Nagaosa, *Phys. Rev.* **B56**, 686 (1997).

[50] M. Imada, *J. Phys. Soc. Jpn.* **67**, 45 (1998).

[51] A. Barnabe, A. Maignan, M. Hervieu, F. Damay, C. Martin, B. Raveau, *Appl. Phys. Lett.* **71**, 3907 (1997).

[52] T. Kimura, Y. Tomioka, R. Kumai, Y. Okimoto, Y. Tokura, *Phys. Rev. Lett.* **83**, 3940 (1997).

[53] M. Uehara, S. Mori, C.H. Chen, S.W. Cheong, *Nature* **399**, 560 (1999).